nature

https://doi.org/10.1038/s41586-023-06849-0

Accelerated Article Preview

SO_2, silicate clouds, but no CH_4 detected in a warm Neptune

Received: 23 June 2023

Accepted: 8 November 2023

Accelerated Article Preview

Cite this article as: Dyrek, A. et al. SO_2, silicate clouds, but no CH_4 detected in a warm Neptune. *Nature* https://doi.org/10.1038/s41586-023-06849-0 (2023)

Achrène Dyrek, Michiel Min, Leen Decin, Jeroen Bouwman, Nicolas Crouzet, Paul Mollière, Pierre-Olivier Lagage, Thomas Konings, Pascal Tremblin, Manuel Güdel, John Pye, Rens Waters, Thomas Henning, Bart Vandenbussche, Francisco Ardevol Martinez, Ioannis Argyriou, Elsa Ducrot, Linus Heinke, Gwenael Van Looveren, Olivier Absil, David Barrado, Pierre Baudoz, Anthony Boccaletti, Christophe Cossou, Alain Coulais, Billy Edwards, René Gastaud, Alistair Glasse, Adrian Glauser, Thomas P. Greene, Sarah Kendrew, Oliver Krause, Fred Lahuis, Michael Mueller, Goran Olofsson, Polychronis Patapis, Daniel Rouan, Pierre Royer, Silvia Scheithauer, Ingo Waldmann, Niall Whiteford, Luis Colina, Ewine F. van Dishoeck, Göran Ostlin, Tom P. Ray & Gillian Wright

SO_2, silicate clouds, but no CH_4 detected in a warm Neptune

November 8, 2023

Achrène Dyrek[1,⋆,†], Michiel Min[2,†], Leen Decin[3,†], Jeroen Bouwman[4], Nicolas Crouzet[5], Paul Mollière[4], Pierre-Olivier Lagage[6], Thomas Konings[3], Pascal Tremblin[7], Manuel Güdel[8,4,9], John Pye[10], Rens Waters[11,12,2], Thomas Henning[4], Bart Vandenbussche[3], Francisco Ardevol Martinez[13,2,14,15], Ioannis Argyriou[3], Elsa Ducrot[6], Linus Heinke[3,14,15], Gwenael Van Looveren[8], Olivier Absil[16], David Barrado[17], Pierre Baudoz[18], Anthony Boccaletti[18], Christophe Cossou[19], Alain Coulais[6,20], Billy Edwards[2], René Gastaud[19], Alistair Glasse[21], Adrian Glauser[9], Thomas P. Greene[22], Sarah Kendrew[23], Oliver Krause[4], Fred Lahuis[2], Michael Mueller[13], Goran Olofsson[24], Polychronis Patapis[9], Daniel Rouan[17], Pierre Royer[3], Silvia Scheithauer[4], Ingo Waldmann[25], Niall Whiteford[26], Luis Colina[17], Ewine F. van Dishoeck[5], Göran Ostlin[27], Tom P. Ray[28], Gillian Wright[29]

[†]Equal contribution is indicated by shared first-authorship.

1. Université Paris Cité, Université Paris-Saclay, CEA, CNRS, AIM, F-91191 Gif-sur-Yvette, France
2. SRON Netherlands Institute for Space Research, Niels Bohrweg 4, 2333 CA Leiden, the Netherlands
3. Institute of Astronomy, KU Leuven, Celestijnenlaan 200D, 3001 Leuven, Belgium
4. Max-Planck-Institut für Astronomie (MPIA), Königstuhl 17, 69117 Heidelberg, Germany
5. Leiden Observatory, Leiden University, P.O. Box 9513, 2300 RA Leiden, the Netherlands
6. Université Paris-Saclay, Université Paris Cité, CEA, CNRS, AIM, F-91191 Gif-sur-Yvette, France
7. Université Paris-Saclay, UVSQ, CNRS, CEA, Maison de la Simulation, 91191, Gif-sur-Yvette, France.
8. Department of Astrophysics, University of Vienna, Türkenschanzstrasse 17, 1180 Vienna, Austria
9. ETH Zürich, Institute for Particle Physics and Astrophysics, Wolfgang-Pauli-Strasse 27, 8093 Zürich, Switzerland
10. School of Physics & Astronomy, Space Research Centre, Space Park Leicester, University of Leicester, 92 Corporation Road, Leicester, LE4 5SP, UK

11. Department of Astrophysics/IMAPP, Radboud University, PO Box 9010, 6500 GL Nijmegen, the Netherlands

12. HFML - FELIX. Radboud University PO box 9010, 6500 GL Nijmegen, the Netherlands

13. Kapteyn Institute of Astronomy, University of Groningen, Landleven 12, 9747 AD Groningen, the Netherlands

14. Centre for Exoplanet Science, University of Edinburgh, Edinburgh, EH9 3FD, UK

15. School of GeoSciences, University of Edinburgh, Edinburgh, EH9 3FF, UK

16. STAR Institute, Université de Liège, Allée du Six Août 19c, 4000 Liège, Belgium

17. Centro de Astrobiología (CAB), CSIC-INTA, ESAC Campus, Camino Bajo del Castillo s/n, 28692 Villanueva de la Cañada, Madrid, Spain

18. LESIA, Observatoire de Paris, CNRS, Université Paris Diderot, Université Pierre et Marie Curie, 5 place Jules Janssen, 92190 Meudon, France

19. Université Paris-Saclay, CEA, Département d'Electronique des Détecteurs et d'Informatique pour la Physique, 91191, Gif-sur-Yvette, France.

20. LERMA, Observatoire de Paris, Université PSL, Sorbonne Université, CNRS, Paris, France

21. UK Astronomy Technology Centre, Royal Observatory, Blackford Hill, Edinburgh EH9 3HJ, UK

22. Space Science and Astrobiology Division, NASA's Ames Research Center, M.S. 245-6, Moffett Field, 94035, California, USA

23. European Space Agency, Space Telescope Science Institute, Baltimore, Maryland, USA

24. Department of Astronomy, Stockholm University, AlbaNova University Center, 10691 Stockholm, Sweden

25. Department of Physics and Astronomy, University College London, Gower Street, WC1E 6BT, UK

26. Department of Astrophysics, American Museum of Natural History, New York, NY 10024, USA

27. Department of Astronomy, Oskar Klein Centre, Stockholm University, 106 91 Stockholm, Sweden

28. School of Cosmic Physics, Dublin Institute for Advanced Studies, 31 Fitzwilliam Place, Dublin, D02 XF86, Ireland

29. UK Astronomy Technology Centre, Royal Observatory Edinburgh, Blackford Hill, Edinburgh EH9 3HJ, UK

Abstract

WASP-107b is a warm ($\sim$740 K) transiting planet with a Neptune-like mass of $\sim$30.5 $M_\oplus$ and Jupiter-like radius of $\sim$0.94 R_J [1, 2] whose extended atmosphere is eroding [3]. Previous observations showed evidence for water vapour and a thick high-altitude condensate layer in WASP-107b's atmosphere [4, 5]. Recently, photochemically produced sulphur dioxide (SO_2) was detected in the atmosphere of a hot ($\sim$1,200 K) Saturn-mass planet from transmission spectroscopy near 4.05 μm [6, 7], but for temperatures below $\sim$1,000 K sulphur is predicted to preferably form sulphur allotropes instead of SO_2 [8, 9, 10]. Here we report the 9σ-detection of two fundamental vibration bands of SO_2, at 7.35 μm and 8.69 μm, in the transmission spectrum of WASP-107b using the Mid-Infrared Instrument (MIRI) of the JWST. This discovery establishes WASP-107b as the second irradiated exoplanet with confirmed photochemistry, extending the temperature range of exoplanets exhibiting detected photochemistry from $\sim$1,200 K down to $\sim$740 K. Additionally, our spectral analysis reveals the presence of silicate clouds, which are strongly favoured ($\sim$7σ) over simpler cloud setups. Furthermore, water is detected ($\sim$12σ), but methane is not. These findings provide evidence of disequilibrium chemistry and indicate a dynamically active atmosphere with a super-solar metallicity.

WASP-107b was observed with JWST MIRI on 19 – 20 January 2023. The `SLITLESSPRISM` subarray of the low-resolution spectrometer was used, offering a spectral resolution ranging from 30 and 100 over a wavelength span of 4.61 to 11.83 μm. We performed three independent data reductions using the `CASCADe` [11], `Eureka!` [12], and `TEATRO` packages; see Supplementary Information (SI). Each method extracted 51 spectroscopic light curves. For all channels, we obtained a minimal level of correlated noise in the residuals, consistent with normally distributed noise. The 1σ error displayed a minimum of 80 ppm at 7.5 μm. The transmission spectra derived from the different reductions, shown in Figure 1 and tabulated in Extended Data Table 1, are within 3σ agreement and 95% of the points within 2σ; see SI.

We performed atmospheric retrievals using two independent frameworks, `ARCiS` [13] and `petitRADTRANS (pRT)` [14], including both our JWST data and previous near-infrared (1.121 – 1.629 μm) HST data [4]. Free abundance retrievals were run including the following species: H_2O, CO, CO_2, CH_4, C_2H_2, SO_2, SO, H_2S, SiO, HCN, NH_3, and PH_3. The remaining atmosphere consisted of H_2 and He. A variety of cloud models were tested, ranging from cloud-free to more complex models, the latter focusing mostly on silicate clouds ($MgSiO_3$, SiO_2, and SiO); see SI.

Figure 2 shows the best fit to the data, including main contributions from molecular species and clouds to the spectrum. The figure presents the results based on the `CASCADe` package, but our conclusions are consistent across the three data reductions. Both retrieval codes detect SO_2 at $\sim$9σ, H_2O at $\sim$12σ, and the presence of high-altitude clouds at $\sim$9σ, with a $\sim$7σ preference for silicate clouds over more simple cloud setups. We also tentatively detect H_2S ($\sim$4σ), NH_3 ($\sim$2 – 3σ), and CO ($\sim$2 – 3σ), although the CO detection relies on the first three spectral points and requires confirmation at shorter wavelengths. CH_4 is not detected, with an upper limit of its volume mixing ratio (VMR) being a few times 10^{-6}. Table 1 presents the detection significance and VMR for each species. Due to differences in cloud structure setups, the absolute VMRs are different between the two retrieval codes. We therefore focus the discussion on the detection significance and relative abundances.

The MIRI data of WASP-107b presents the mid-infrared discovery of SO_2 in an exoplanet atmosphere. Both the ν_1 symmetric stretch and the ν_3 asymmetric stretch vibration bands of SO_2 (with fundamental frequency at 8.69 μm and 7.35 μm, respectively [15]) are detected (Figure 1 and Figure 2). Recently, the $(\nu_1 + \nu_3)$ combination band of SO_2 was assigned as carrier of a spectral feature near 4.05 μm detected in the JWST NIRspec spectrum of WASP-39b[6, 16], a hot (∼1,200 K) irradiated Saturn-mass exoplanet. The MIRI detection of SO_2 in WASP-107b extends the range of exoplanet temperatures with detected SO_2 from ∼1,200 K down to ∼740 K.

The measured VMR of SO_2 in WASP-107b (see Table 1) is several orders of magnitude higher than expected for chemical equilibrium, which predicts H_2S to be the dominant sulphur-bearing molecule for Neptune-like planets [9]. Disequilibrium processes can drive abundances considerably away from chemical equilibrium, with photochemistry and atmospheric transport being the dominant mechanisms [17]. Notably, the SO_2 feature observed in WASP-39b has been attributed to photochemical processes occurring within its atmosphere [10]. Indeed, UV irradiation initiates the photodissociation of H_2O, yielding H and OH radicals. These OH radicals are key for oxidising sulphur that is liberated from H_2S [10]. However, these models[10] predict that SO_2 would not be detectable using JWST MIRI for a planet with an equilibrium temperature of ∼740 K. This is in contrast with our detection of SO_2 in the atmosphere of WASP-107b.

To unravel the production paths of SO_2 in WASP-107b, we computed a grid of disequilibrium models (see SI). To ensure an accurate consideration of the upper-atmosphere chemistry, we observed – contemporaneously with the JWST observations – the Near-Ultraviolet (NUV) emission of the host star WASP-107 with *Neil Gehrels Swift*. Additionally, we reanalysed the 2018 X-ray emission observed with *XMM-Newton* (see SI). Figure 3 provides evidence that only models incorporating photochemistry in combination with a super-solar metallicity predict a detectable level of SO_2 in WASP-107b. Key disparities from prior predictions [10, 17] stem from UV radiation and gravity. Previous models adopted a gravity of 1,000 cm/s^2 [10] and 2,140 cm/s^2 [17], while WASP-107b's gravity is ∼260 cm/s^2. Moreover, the NUV flux is a factor ∼200 lower for WASP-107b than for WASP-39b, and a factor ∼100 − 1,000 lower in the FUV (see SI). A lower gravity, an overall decreased UV flux, and a low FUV/NUV ratio collectively contribute to the increased formation of SO_2; see Extended Data Figure 1.

The overarching scenario that unfolds is that the initiating pathways for SO_2 formation in WASP-107b are twofold. First, H_2O photodissociation in upper layers at pressures $\lesssim 10^{-5}$ bar generates atomic H and OH radicals, leading to sequential oxidation of sulphur liberated from H_2S. Second, in the pressure range of $\sim 10^{-5} - 1$ bar, photolysis of various abundant molecules – beyond just H_2O – provides free atoms and radicals, partially redistributed through eddy diffusion. This initiates a cascade of thermochemical reactions that progressively yield sufficient OH radicals for SO_2 oxidation. Given the fact that a large fraction of these reactions are temperature-independent and barrierless, the equilibrium temperature is not the sole determinant for SO_2 formation. As long as the UV irradiation and FUV/NUV ratio remain moderate and the gravity is low, these processes lead to detectable SO_2 levels even at the low equilibrium temperature of WASP-107b.

The sensitivity to metallicity can be attributed to the larger abundance of sulphur and OH radicals at higher metallicities. At a metallicity of 6× solar, the SO_2 spectral features contribute partially to the 7.8 μm feature and dominate at $\gtrsim$10× solar (see Extended Data Figure 2). For metallicities ≥6× solar, the gas-phase photochemical models predict a SO_2 VMR above $\sim 5\times10^{-7}$

at pressures between $10^{-7}-10^{-4}$ bar (see Figure 3). This result is corroborated by the retrieval outcomes, which show that the spectral contribution of SO_2 predominantly comes from the region above the high-altitude cloud layer (situated at pressures of a few times 10^{-5} bar; see Extended Data Figure 4). This establishes SO_2 as a key diagnostic for the atmospheric metallicity in exoplanet atmospheres.

At super-solar metallicity, our models also predict a detectable CH_4 feature (see Extended Data Figure 2). The confirmation of the HST CH_4 non-detection [4] in the MIRI wavelength range raises questions regarding the predicted predominance of CH_4 in the atmosphere [18, 19]. One potential reason for the non-detection of CH_4 is that it is hidden by the high-altitude cloud layer. In contrast to SO_2, CH_4 is photochemically destroyed at high altitudes, i.e. above the cloud layer (see Extended Data Figure 3). Another explanation for the non-detection of CH_4 is the influence of the strong irradiation experienced by WASP-107b, which can significantly impact the thermodynamical properties of its atmosphere [20, 21, 22]. WASP-107b is highly inflated, pointing to a deep atmosphere that has significantly higher temperatures [23, 24, 25, 26] than those predicted by conventional models. The latter suggest an intrinsic heat flux ($\sigma T_{\rm int}^4$, with σ the Boltzmann constant and $T_{\rm int}$ the intrinsic temperature) with corresponding $T_{\rm int}$ of 150 K [27]. We computed chemical models with different intrinsic temperatures ranging from 250 – 600 K to reproduce a hot deep atmosphere (see Extended Data Figure 3). Our results show that the CH_4 molar fraction in the atmospheric layers probed by our MIRI observations is reduced by more than 3 orders-of-magnitude when we increase $T_{\rm int}$ from 250 to 600 K. Interestingly, the SO_2 abundance in the detectable upper atmosphere is almost unaffected since sulphur species do not quench in deep regions [9] (see Extended Data Figure 3). Lowering the C/O ratio from solar (= 0.55) to 0.10 yields an additional decrease of the CH_4 abundance by a factor ∼15 (see Extended Data Figure 3).

The presence of silicate clouds in the atmospheres of strongly irradiated planets has been predicted for a long time [28]. Although a hint of silicate emission has been claimed for one single object [29], clear observational evidence has been lacking. Recently, silicate clouds were detected in a young, self-luminous planet at large separation from its host star [30]. The MIRI data of WASP-107b present the detection of the 10 μm Si-O stretching mode of solid silicate particles. The retrieval models favour a high-altitude cloud layer composed of small (sub-micron) amorphous silicate particles. At the pressure levels and temperatures where we find the cloud layer, gas phase SiO can nucleate and condensate efficiently to form small solid state mineral particles [31]. However, according to the traditional picture on cloud formation, these particles would eventually rain down to deeper, hotter layers of the atmosphere, depleting the relatively cold upper atmosphere from gas phase SiO. In the deeper, hotter layers, the particles evaporate, allowing the gas phase material to mix and serve as building blocks for new nucleation/condensation cycles. Thus, we can conclude that the presence of silicate clouds at such high altitudes in a relatively cold part of the atmosphere is another indication of strong mixing from either a hot inner atmosphere (similar to the finding related to CH_4) or potentially from the intensely irradiated hot dayside.

Figure 1: **JWST MIRI transmission spectrum of WASP-107b.** Comparison of the JWST MIRI transmission spectra obtained from the three independent reductions considered in this work (coloured points, with 1-σ error bars). The blue dots show the results from the `CASCADe` code, the red dots using the `Eureka!` package and the black dots are from the `TEATRO` routines. The thick dashed grey line indicates the band-averaged transit depth from the `CASCADe` analysis at 20,463 ppm and the shaded area the 95% confidence interval of 39 ppm. The right y-axis gives the planetary spectrum in units of atmospheric scale height of the planetary atmosphere, assuming a hydrogen dominated atmosphere. The spectra have a constant wavelength bin width, corresponding to a spectral resolution of 50 at 7.5 μm. The two horizontal bars indicate the ν_1 symmetric stretch and ν_3 asymmetric stretch vibration bands of SO_2.

Figure 2: **Transmission spectrum of WASP-107b with key contributions.** The (red and pink) points with 1-σ error bars correspond to the measured JWST MIRI `CASCAde` transit depths of the spectrophotometric light curves at different wavelengths. The (red and pink) points in the area indicated by the grey band are from HST. The median spectrum model predicted from `ARCiS` [13] retrievals is shown in blue and from `petitRADTRANS (pRT)` [14] in green (offset by 2,000 ppm for clarity). The shaded regions of the model spectra correspond to the 1-,2-,3-σ credibility envelopes predicted by the retrievals. The bottom part of the figure shows the silicate cloud and molecular contributions for those gases inferred by our analysis of WASP-107b's spectrum.

Figure 3: **Predicted SO_2 molar fraction.** Panel (a): Adopted temperature-pressure (T-P) profile for WASP-107b following the analytical equation of ref. [32]; see SI. Panel (b): Predicted SO_2 molar fraction for four values of the metallicity (1, 2, 6, and 10 $Z_\odot$; in black, green, red, and blue, respectively) for models with (full line) and without (dotted line) the inclusion of photochemistry. Predictions are calculated for a model with an intrinsic temperature of 400 K, a solar C/O ratio, and a $\log_{10}(K_{zz}, \text{cgs}) = 10$.

Table 1: **Outcome of the retrieval analyses.** Given are the detection significance and volume mixing ratios (VMR) of the various components in the `ARCiS` and `petitRADTRANS` (`pRT`) retrieval analysis.

	Significance $[\sigma]$		$\log_{10}$(VMR)	
Component	`ARCiS`	`pRT`	`ARCiS`	`pRT`
H_2O	13.2	12.5	$-2.19^{+0.42}_{-0.26}$	$-3.81^{+0.38}_{-0.29}$
SO_2	8.8	9.1	$-5.03^{+0.33}_{-0.18}$	$-6.72^{+0.30}_{-0.23}$
H_2S	4.7	3.5	$-2.65^{+0.49}_{-0.38}$	$-3.88^{+0.41}_{-0.33}$
NH_3	2.3	3.4	$-5.47^{+0.34}_{-0.66}$	$-6.04^{+0.30}_{-0.25}$
CO	2.8	2.3	$-2.41^{+0.29}_{-0.28}$	$-4.58^{+0.40}_{-0.59}$
PH_3	–[b]	–[a]	$-6.29^{+1.29}_{-2.24}$	$-7.60^{+0.89}_{-1.39}$
HCN	–[b]	–[a]	$-9.26^{+1.73}_{-1.63}$	$-9.19^{+1.20}_{-1.15}$
C_2H_2	–[b]	–[a]	$-9.08^{+1.73}_{-1.73}$	$-9.19^{+1.19}_{-1.14}$
SiO	–[b]	–[a]	$-6.08^{+1.90}_{-3.34}$	$-9.03^{+1.47}_{-1.40}$
CH_4	–[b]	–[b]	$-8.52^{+2.09}_{-2.09}$	$-8.83^{+1.25}_{-1.23}$
CO_2	–[b]	–[b]	$-8.05^{+2.46}_{-2.37}$	$-8.49^{+1.79}_{-1.70}$
SO	–[b]	–[c]	$-7.38^{+2.76}_{-2.74}$	
Silicate Clouds	7.2	7.1		

[a] included in retrieval, but not tested for detection significance because posterior indicates an upper limit.
[b] not favoured (Bayes factor < 2).
[c] not included.

- **Supplementary Information** is linked to the online version of the paper at www.nature.com/nature.
- **Data availability.** The JWST MIRI data presented in this paper are part of the JWST MIRI GTO program (Program identifier (PID) 1280; P.I. P.O. Lagage). The JWST data will be publicly available in the Barbara A. Mikulski Archive for Space Telescopes (MAST; https://archive.stsci.edu/) after January 20, 2024, and can be found either using the program identifier or using the Data Object Identifier (DOI): https://doi.org/10.17909/as3s-x893. The DOI link can also be used to retrieve the publicly available HST WFC3 data used in this paper from MAST. The NUV data are in an online publicly-accessible archive: https://heasarc.gsfc.nasa.gov/cgi-bin/W3Browse/swift.pl. The HST data are available in the MAST archive and can be found using DOI: https://doi.org/10.17909/as3s-x893. The XMM X-ray data archive is available at https://nxsa.esac.esa.int/nxsa-web/#search.
- **Code availability.** The codes used in this publication to extract, reduce, and analyse the data are as follows. The data reduction pipeline `jwst` can be found at https://jwst-pipeline.readthedocs.io/en/latest/. The data analysis codes `Eureka!`, `CASCADe`, and `TEATRO` can be found respectively at https://eurekadocs.readthedocs.io/en/latest/, https://gitlab.com/jbouwman/CASCADe, and https://github.com/ncrouzet/TEATRO. The `CASCADe-filtering`, and `CASCADe-jitter` sub-packages can be found, respectively, at https://gitlab.com/jbouwman/CASCADe-filtering, and https://gitlab.com/jbouwman/CASCADe-jitter. The atmospheric model codes used to fit the data can be found at https://www.exoclouds.com/ for the `ARCiS`-code [13] and at https://petitradtrans.readthedocs.io/en/latest/ for the `petitRADTRANS`-code [14]. The XSPEC package [33] is available at https://heasarc.gsfc.nasa.gov/xanadu/xspec/. The HEASoft package (including the Swift UVOT tools) is available at https://heasarc.gsfc.nasa.gov/lheasoft/download.html (version 6.31.1 was used in our work). The NUV *Swift*-project pipeline is available at https://swift.gsfc.nasa.gov/quicklook/swift_process_overview.html. The VULCAN chemical network can be found at https://github.com/exoclime/VULCAN/blob/master/thermo/SNCHO_photo_network.txt.
- **Inclusion & Ethics.** All authors have committed to upholding the principles of research ethics & inclusion as advocated by the Nature Portfolio journals.
- **Acknowledgments.** This work is based on observations made with the NASA/ESA/CSA JWST. The data were obtained from the Mikulski Archive for Space Telescopes at the Space Telescope Science Institute, which is operated by the Association of Universities for Research in Astronomy, Inc., under NASA contract NAS 5-03127 for JWST. These observations are associated with program 1280. MIRI draws on the scientific and technical expertise of the following organisations: Ames Research Center, USA; Airbus Defence and Space, UK; CEA-Irfu, Saclay, France; Centre Spatial de Liège, Belgium; Consejo Superior de Investigaciones Científicas, Spain; Carl Zeiss Optronics, Germany; Chalmers University of Technology, Sweden; Danish Space Research Institute, Denmark; Dublin Institute for Advanced Studies, Ireland; European Space Agency, Netherlands; ETCA, Belgium; ETH Zurich, Switzerland; Goddard Space Flight Center, USA; Institut d'Astrophysique Spatiale, France; Instituto Nacional de Técnica Aeroespacial, Spain; Institute for Astronomy, Edinburgh, UK; Jet

Propulsion Laboratory, USA; Laboratoire d'Astrophysique de Marseille (LAM), France; Leiden University, Netherlands; Lockheed Advanced Technology Center (USA); NOVA Opt-IR group at Dwingeloo, Netherlands; Northrop Grumman, USA; Max-Planck Institut für Astronomie (MPIA), Heidelberg, Germany; Laboratoire d'Etudes Spatiales et d'Instrumentation en Astrophysique (LESIA), France; Paul Scherrer Institut, Switzerland; Raytheon Vision Systems, USA; RUAG Aerospace, Switzerland; Rutherford Appleton Laboratory (RAL Space), UK; Space Telescope Science Institute, USA; Toegepast Natuurwetenschappelijk Onderzoek (TNO-TPD), Netherlands; UK Astronomy Technology Centre, UK; University College London, UK; University of Amsterdam, Netherlands; University of Arizona, USA; University of Bern, Switzerland; University of Cardiff, UK; University of Cologne, Germany; University of Ghent; University of Groningen, Netherlands; University of Leicester, UK; University of Leuven, Belgium; University of Stockholm, Sweden; Utah. The following National and International Funding Agencies funded and supported the MIRI development: NASA; ESA; Belgian Science Policy Office (BELSPO); Centre Nationale d'Etudes Spatiales (CNES); Danish National Space Centre; Deutsches Zentrum fur Luftund Raumfahrt (DLR); Enterprise Ireland; Ministerio De Economalia y Competividad; Netherlands Research School for Astronomy (NOVA); Netherlands Organisation for Scientific Research (NWO); Science and Technology Facilities Council; Swiss Space Office; Swedish National Space Agency; and UK Space Agency. C.C., A.D. P.-O.L. R.G. A.C. acknowledge funding support from CNES. O.A. I.A. B.V. and P.R. thank the European Space Agency (ESA) and the Belgian Federal Science Policy Office (BELSPO) for their support in the framework of the PRODEX Programme. D.B. is supported by Spanish MCIN/AEI/10.13039/501100011033 grant PID2019-107061GB-C61 and and No. MDM-2017-0737. L.D. acknowledges funding from the KU Leuven Interdisciplinary Grant (IDN/19/028), the European Union H2020-MSCA-ITN-2019 under Grant no. 860470 (CHAMELEON) and the FWO research grant G086217N. I.K. acknowledges support from grant TOP-1 614.001.751 from the Dutch Research Council (NWO). O.K. acknowledges support from the Federal Ministery of Economy (BMWi) through the German Space Agency (DLR). J.P.P. acknowledges financial support from the UK Science and Technology Facilities Council, and the UK Space Agency, and acknowledges the advice of the *Swift* project team, and especially Kim Page (UK Swift Science Data Centre at University of Leicester) in planning and analysis of the *Swift* observations. G.O. acknowledge support from the Swedish National Space Board and the Knut and Alice Wallenberg Foundation. P.T. acknowledges support by the European Research Council under Grant Agreement ATMO 757858. I.P.W. acknowledges funding from the European Research Council (ERC) under the European Union's Horizon 2020 research and innovation programme (grant agreement No 758892, ExoAI), from the Science and Technology Funding Council grants ST/S002634/1 and ST/T001836/1 and from the UK Space Agency grant ST/W00254X/1. F.A.M. has received funding from the European Union's Horizon 2020 research and innovation programme under the Marie Skłodowska-Curie grant agreement no. 860470. E.D. has received funding from the European Union's Horizon 2020 research and innovation programme under the Marie Skłodowska-Curie actions Grant Agreement no 945298-ParisRegionFP. G.V.L. acknowledges that some results of this work were partially achieved at the Vienna Scientific Cluster (VSC). L.H. has received funding from the European Union's Horizon 2020 research and innovation program under the Marie Skłodowska-Curie grant agreement no. 860470. T.K. acknowledges funding from the KU Leuven Interdisciplinary Grant (IDN/19/028). L.C. acknowledges support by grant PIB2021-127718NB-100 from the Spanish Ministry of Science and Innovation/State Agency of Research MCIN/AEI/10.13039/501100011033. E.vD. acknowledges support from A-ERC grant 101019751 MOLDISK. T.P.R. acknowledges support from the ERC 743029 EASY. G.O. acknowledges support from SNSA. P.P. thanks the Swiss National Science Foundation (SNSF) for financial support under grant number 200020_200399. O.A. is a Senior Research Associate of the Fonds de la Recherche Scientifique - FNRS. We thank Luis Welbanks for a fruitful discussion on the significance of the retrieval results. We thank Olivia Venot for sharing with us the new sulphur photo-absorption cross-sections and Robin Baeyens for implementing them and the VULCAN thermo-chemical network in our full chemical network. We thank the MIRI instrument team and the many other people who contributed to the success of JWST.

- **Author Contributions.** All authors played a significant role in one or more of the following: development of the original proposal, management of the project, definition of the target list and observation plan, analysis of the data, theoretical modelling and preparation of this paper. Some specific contributions are listed as follows. P.-O.L. is PI of the JWST MIRI GTO European consortium program dedicated to JWST observations of exoplanet atmospheres; R.W. is co-lead of this JWST MIRI GTO European consortium. L.D. and N.C. provided overall program leadership and management of the WASP-107b working group. P.-O.L., J.B., T.H., R.W., T.G. and L.D. made significant contributions to the design of the observational program and contributed to the setting of the observing parameters. A.D., J.B. and N.C. generated simulated data for prelaunch testing of the data reduction methods. J.B., A.D., and N.C. reduced the data, modelled the light curves and produced the planetary spectrum. P.T., T.K., and L.D. generated theoretical model grids for comparison with the data. M.Mi. and P.M. fitted the generated spectrum with retrieval models. J.P. led the associated *Swift* observing programme and performed the analysis of the *Swift* data. M.G. led the data reduction and the analysis of the *XMM-Newton* X-ray data. L.D., M.Mi, J.B., and A.D. led the writing of the manuscript. L.D., A.D., M.Mi., P.M., J.B., N.C., T.K., J.P., M.G., R.W., P.T., and P.-O.L. made significant contributions to the writing of this paper. T.K., M.Mi., J.B., and P.M. generated figures for this paper. G.W. is the European PI of the JWST MIRI instrument, P.-O.L., T.H., M.G, B.V., L.C., E.vD., T.R., and G.O. are European co-PI, and L.D., R.W., O.A., I.K., O.K., J.P., G.O. and D.B. are European co-I of the JWST MIRI instrument. A.G. led the MIRI instrument testing and commissioning effort.

- **Author Information.** *Correspondence and requests for materials should be addressed to achrene.dyrek@cea.fr.

- **Competing Interests.** The authors declare that they have no competing financial interests.

References

[1] Anderson, D. R. *et al.* The discoveries of WASP-91b, WASP-105b and WASP-107b: Two warm Jupiters and a planet in the transition region between ice giants and gas giants. *Astron. Astrophys.* **604**, A110 (2017).

[2] Piaulet, C. *et al.* WASP-107b's Density Is Even Lower: A Case Study for the Physics of Planetary Gas Envelope Accretion and Orbital Migration. *Astron. J.* **161** (2), 70 (2021).

[3] Spake, J. J. *et al.* Helium in the eroding atmosphere of an exoplanet. *Nature* **557**, 68-70 (2018).

[4] Kreidberg, L. *et al.* Water, High-altitude Condensates, and Possible Methane Depletion in the Atmosphere of the Warm Super-Neptune WASP-107b. *Astrophys. J.* **858** (1), L6 (2018).

[5] Edwards, B. *et al.* Exploring the Ability of HST WFC3 G141 to Uncover Trends in Populations of Exoplanet Atmospheres Through a Homogeneous Transmission Survey of 70 Gaseous Planets. *Astrophys. J.*, (2022).

[6] Rustamkulov, Z. *et al.* Early Release Science of the exoplanet WASP-39b with JWST NIRSpec PRISM. *Nature* **614** (7949), 659–663 (2023).

[7] Alderson, L. *et al.* Early Release Science of the exoplanet WASP-39b with JWST NIRSpec G395H. *Nature* **614** (7949), 664–669 (2023).

[8] Zahnle, K. *et al.* Photolytic Hazes in the Atmosphere of 51 Eri b. *Astrophys. J.* **824** (2), 137 (2016).

[9] Tsai, S. M. *et al.* A Comparative Study of Atmospheric Chemistry with VULCAN. *Astrophys. J.* **923** (2), 264 (2021).

[10] Tsai, S. M. *et al.* Photochemically produced SO_2 in the atmosphere of WASP-39b. *Nature* **617** (7961), 483-487 (2023).

[11] Bouwman, J. *et al.* Spectroscopic Time Series Performance of the Mid-infrared Instrument on the JWST. *Publ. Astron. Soc. Pacific* **135** (1045), 038002 (2023).

[12] Bell, T.J. *et al.* Eureka!: An End-to-End Pipeline for JWST Time-Series Observations. *The Journal of Open Source Software* **7** (79), 4503 (2022).

[13] Min, M. *et al.* The ARCiS framework for exoplanet atmospheres. Modelling philosophy and retrieval. *Astron. Astrophys.* **642**, A28 (2020).

[14] Mollière, P. *et al.* petitRADTRANS. A Python radiative transfer package for exoplanet characterization and retrieval. *Astron. Astrophys.* **627**, A67 (2019).

[15] Herzberg, G. Molecular spectra and molecular structure. Vol.3: Electronic spectra and electronic structure of polyatomic molecules. *Van Nostrand Reinhold Company*, (1966)

[16] Jakobsen, P. *et al.* The Near-Infrared Spectrograph (NIRSpec) on the James Webb Space Telescope. I. Overview of the instrument and its capabilities. *Astrophys. J.* **661**, A80 (2022).

[17] Polman, J. *et al.* H_2S and SO_2 detectability in hot Jupiters. Sulphur species as indicators of metallicity and C/O ratio. *Astron. Astrophys.* **670**, A161 (2023).

[18] Madhusudhan, N. C/O ratio as a Dimension for Characterizing Exoplanetary Atmospheres. *Astrophys. J.* **758** (1), 36 (2012).

[19] Benneke, B. *et al.* A sub-Neptune exoplanet with a low-metallicity methane-depleted atmosphere and Mie-scattering clouds. *Nature Astronomy* **3** (9), 813–821 (2019).

[20] Cooper, C. S. & Showman, P. Dynamics and Disequilibrium Carbon Chemistry in Hot Jupiter Atmospheres, with Application to HD 209458b. *Astrophys. J.* **649** (2), 1048-1063 (2006).

[21] Showman, A.P *et al.* Atmospheric Circulation of Hot Jupiters: Coupled Radiative-Dynamical General Circulation Model Simulations of HD 189733b and HD 209458b. *Astrophys. J.* **699** (1), 564-584 (2009).

[22] Drummond, B. *et al.* Implications of three-dimensional chemical transport in hot Jupiter atmospheres: Results from a consistently coupled chemistry-radiation-hydrodynamics model *Astron. Astrophys.* **636** (1), A68 (2020).

[23] Showman, A. P. & Guillot, T. tmospheric circulation and tides of "51 Pegasus b-like" planets. *Astron. Astrophys.* **385** (1), 166-180 (2002).

[24] Sainsbury-Martinez, F. *et al.* Idealised simulations of the deep atmosphere of hot Jupiters. Deep, hot adiabats as a robust solution to the radius inflation problem. *Astron. Astrophys.* **632** (1), A114 (2019).

[25] Sarkis,P. *et al.* Evidence of three mechanisms explaining the radius anomaly of hot Jupiters. *Astron. Astrophys.* **645** (1), A79 (2021).

[26] Schneider, A.D. *et al.* No evidence for radius inflation in hot Jupiters from vertical advection of heat. *Astron. Astrophys.* **666** (1), L11 (2022).

[27] Baraffe, I., Chabrier, G. & Barman, T. The physical properties of extra-solar planets. *Reports on Progress in Physics* **73** (1), 016901 (2010).

[28] Seager, S., Whitney, B. A. & Sasselov, D. D. Photometric Light Curves and Polarization of Close-in Extrasolar Giant Planets. *Astrophys. J.* **540**, 504-520 (2000)

[29] Richardson, L. *et al.* A spectrum of an extrasolar planet. *Nature* **445** (7130), 892-895 (2007).

[30] Miles, B. E. *et al.* The JWST Early-release Science Program for Direct Observations of Exoplanetary Systems II: A 1 to 20 μm Spectrum of the Planetary-mass Companion VHS 1256-1257 b. *Astrophys. J. L.* **946** (1), L6 (2023).

[31] Nuth, J. A. & Ferguson, F. T. Silicates Do Nucleate in Oxygen-rich Circumstellar Outflows: New Vapor Pressure Data for SiO. *Astrophys. J.* **649** (2), 1178-1183 (2006).

[32] Guillot, T. On the radiative equilibrium of irradiated planetary atmospheres. *Astron. Astrophys.* **520** (1), A27 (2010).

[33] Arnaud, K. A. XSPEC: The First Ten Years. *Astronomical Society of the Pacific* **101** (1), 17 (1996).

[34] Loyd, R. O. P. *et al.* The MUSCLES Treasury Survey. III. X-Ray to Infrared Spectra of 11 M and K Stars Hosting Planets. *Astrophys. J.* **824** (2), 102 (2016).

Extended Data

Extended Data – Table 1: **Measured transit depth of WASP-107b.** First and fifth column list the wavelength, and the other columns the transit depths as obtained with `Eureka!`, `CASCADe` and `TEATRO`. Each wavelength bin has a full width of 0.15 μm.

Extended Data – Figure 1: **Impact of gravity and UV irradiation on predicted SO_2 molar fraction.** The base model (shown in black in each panel) has an intrinsic temperature of 400 K, a solar C/O ratio, a metallicity of 10× solar, a $\log_{10}(K_{zz}, \mathrm{cgs}) = 10$, and uses the SED of HD 85512 [34] – used as a proxy for WASP-107 – as input stellar spectrum (see SI). Panel (a): Temperature-pressure (T-P) profile for a gravity g of $2.6\,\mathrm{m/s^2}$ (black, purple and brown), $4.3\,\mathrm{m/s^2}$ (blue), and $10\,\mathrm{m/s^2}$ (orange). Panel (b): Predicted SO_2 molar fractions for different gravity values with colours corresponding to panel (a). While the black curve uses the HD 85512 SED as input spectrum, the purple curve uses the WASP-39 SED instead (see SI), and the brown curve the HD 85512 SED scaled with a factor 100.

Extended Data – Figure 2: **Predicted transit depth for WASP-107b assuming a cloudless atmosphere.** The four panels display for a metallicity of 1, 2, 6, and 10 $Z_\odot$, the total transit depth (in black) and the transit depth without relative contributions of SO_2 (light blue), H_2O (dark blue), CO_2 (light green), CH_4 (pink) and NH_3 (orange). Predictions are calculated for a model with an intrinsic temperature of 400 K, a solar C/O ratio, and a $\log_{10}(K_{zz}, \mathrm{cgs}) = 10$.

Extended Data – Figure 3: **Sensitivity of SO_2 and CH_4 molar fractions to various input parameters.** Shown are the impact of the intrinsic temperature, C/O ratio and eddy diffusion coefficient on predicted SO_2 and CH_4 molar fractions. The base model (shown in black in each panel) has an intrinsic temperature of 400 K, a solar C/O ratio, a metallicity of 10× solar, and a $\log_{10}(K_{zz}, \text{cgs}) = 10$. Panel (a): Temperature-pressure (T-P) profile for intrinsic temperatures of 250, 400, and 600 K (light blue, black, and orange, respectively). Panel (b): Predicted SO_2 (full line) and CH_4 (dotted line) molar fractions for different T-P structures (and hence intrinsic temperatures), with colours corresponding to panel (a). Panel (c): Predicted SO_2 and CH_4 molar fraction for different C/O ratios. Comparison with predictions for a solar C/O ratio (of 0.55, black line) for which either the carbon or oxygen atomic abundance has been adapted (indicated by 'C' or 'O' between parenthesis, respectively). Panel (d): Predicted SO_2 and CH_4 molar fraction for different values of the eddy diffusion coefficient K_{zz}.

Extended Data – Figure 4: **Contribution function for the atmosphere as retrieved by `ARCiS`.** Shown in the contour colours are the relative contributions of various layers in the atmosphere to the transit spectrum as a function of wavelength. The dark horizontal line in this plot is located at the geometrically thin cloud layer, dominating the spectrum at all wavelengths. The spectral variation on top of this baseline predominantly comes from below the cloud layer at the wavelengths where water features are present, while it is dominated by regions above the cloud layer for the spectral features of SO_2. This is consistent with the pressures where we expect SO_2 to be abundant in the atmosphere from our photochemical modelling (see Figure 3). The molecular contribution to the spectral variation in the 9.5 – 11 μm region is significantly fainter than at other wavelengths. This is the region where the silicate feature is most prominent and thus also the spectral variation is dominated by the cloud layer.

Extended Data – Figure 5: **Silicate cloud detection significance.** The detection significance, measured in σ, of the silicate cloud model is presented in comparison to both the cloud-free model (indicated by the blue dashed curve) and the parameterised cloud model (represented by the red solid line) as a function of the maximum wavelength used in the analysis. Even when limiting the analysis to wavelengths below 10 μm, the silicate cloud remains favoured, at a significance of 5.7σ, over the parameterised cloud configuration.

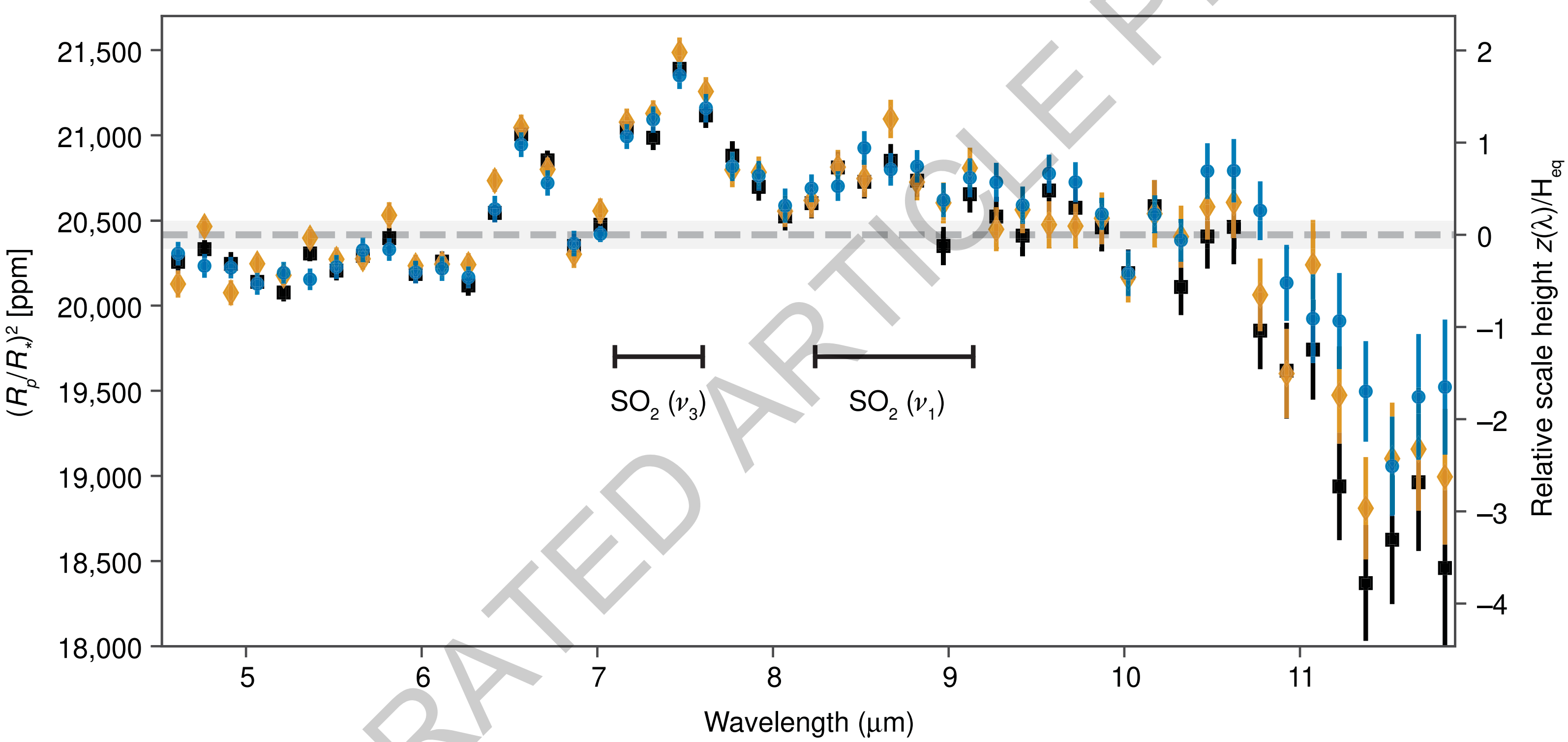

21,500
21,000
20,500
20,000
19,500
19,000
18,500
18,000
(Rp/R*)2 [ppm]
5
6
7
8
9
10
11
Wavelength (µm)
2
1
0
−1
−2
−3
−4
Relative scale height z(λ)/Heq
SO2 (ν3)
SO2 (ν1)

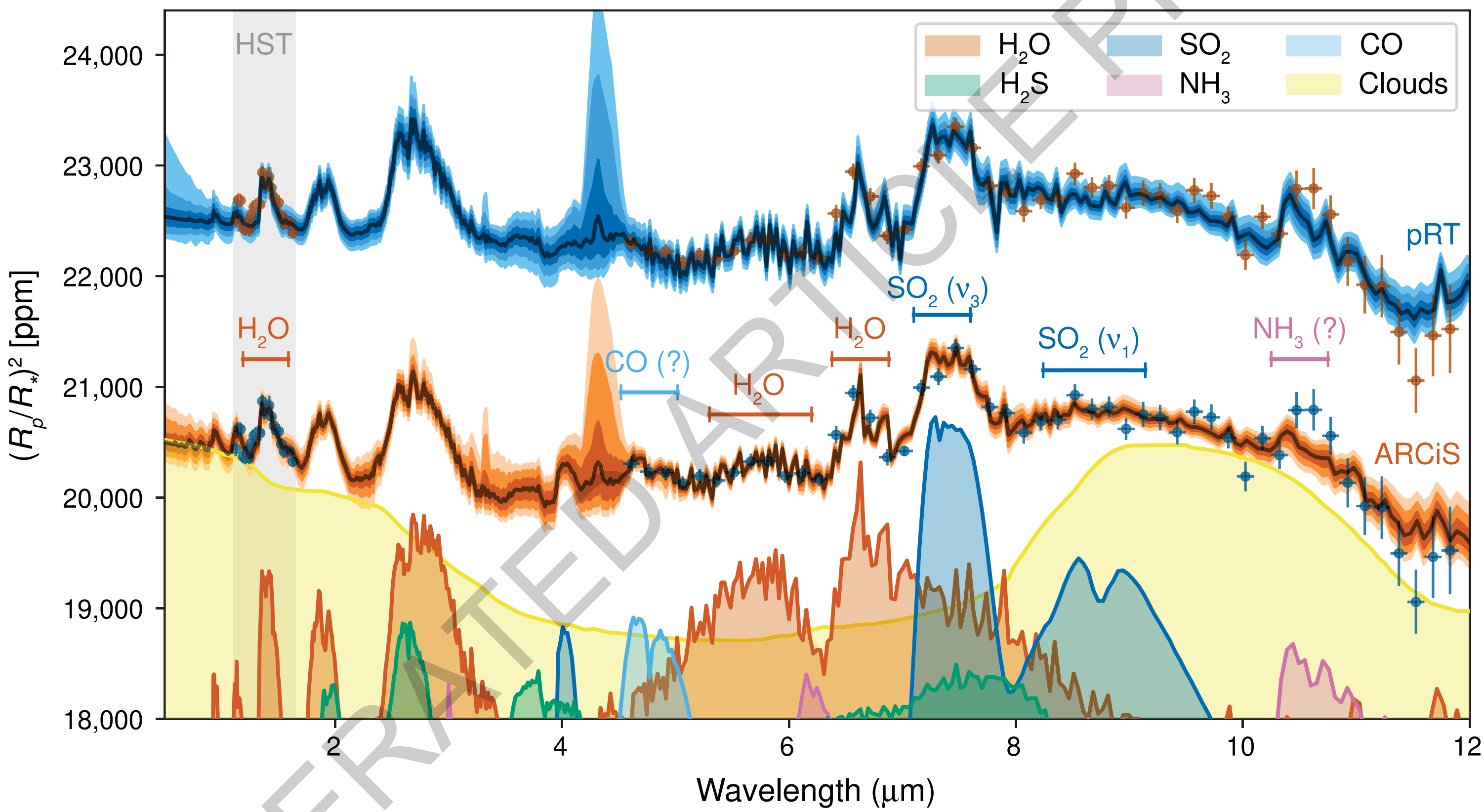

HST
H_2O
SO_2
CO
H_2S
NH_3
Clouds
pRT
ARCiS
H_2O
CO (?)
H_2O
H_2O
SO_2 (ν_3)
SO_2 (ν_1)
NH_3 (?)
24,000
23,000
22,000
21,000
20,000
19,000
18,000
$(R_p/R_*)^2$ [ppm]
2
4
6
8
10
12
Wavelength (μm)

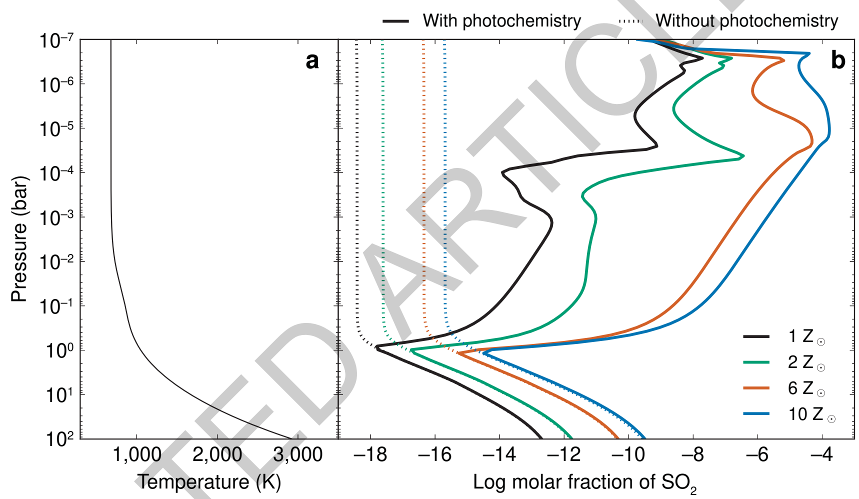
With photochemistry
Without photochemistry
a
b
Pressure (bar)
Temperature (K)
Log molar fraction of SO2
1 Z⊙
2 Z⊙
6 Z⊙
10 Z⊙

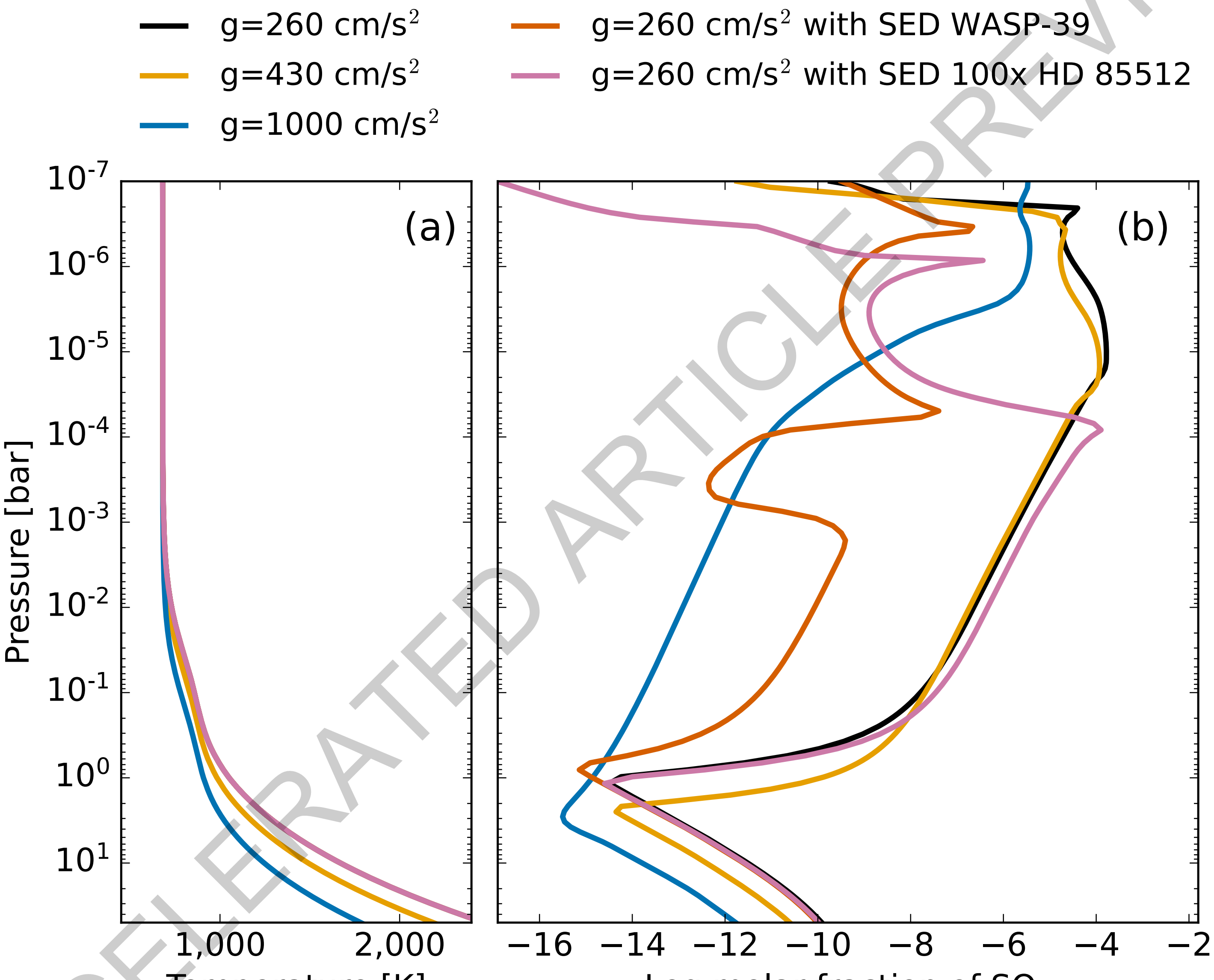

Extended Data Fig. 1

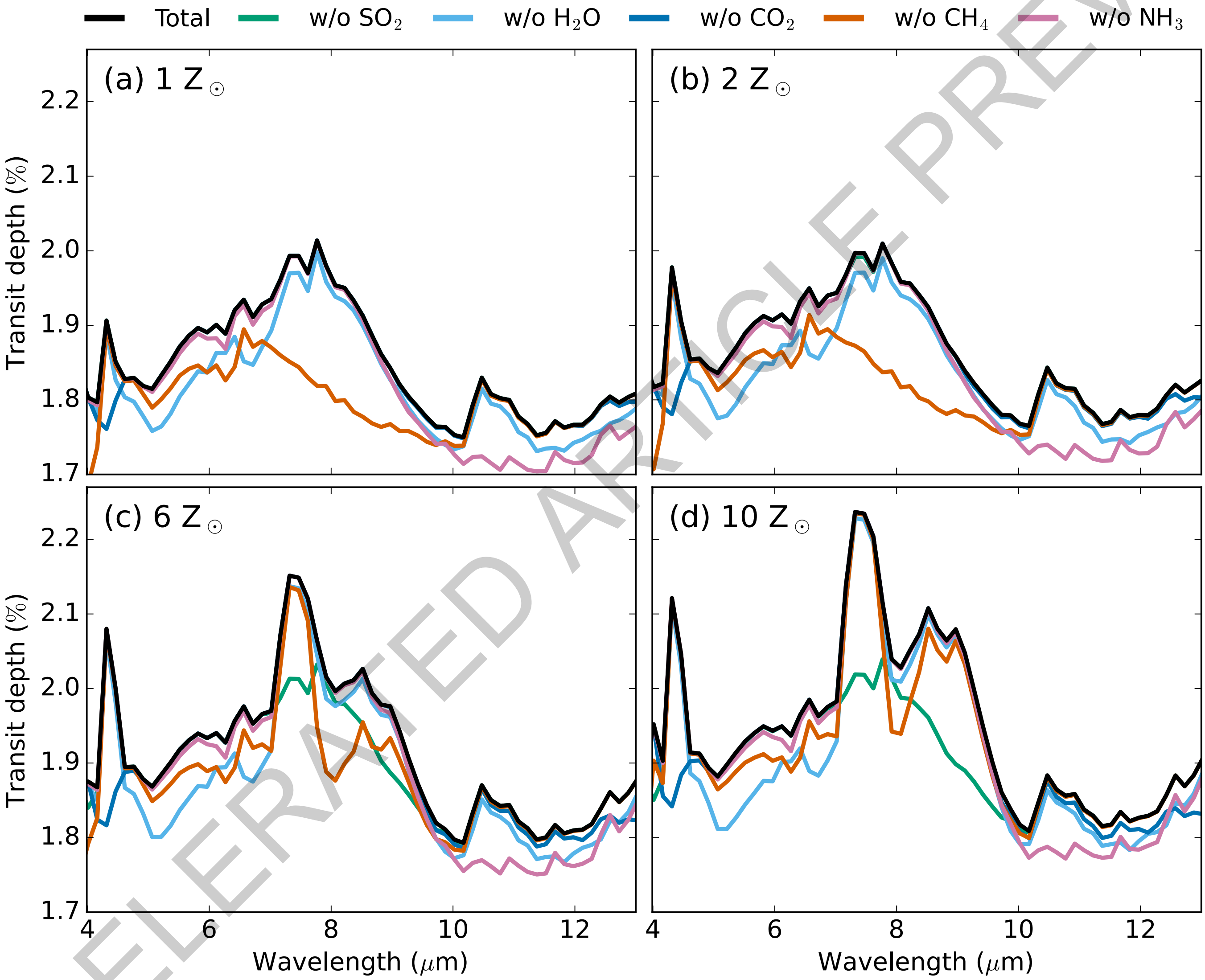

Extended Data Fig. 2

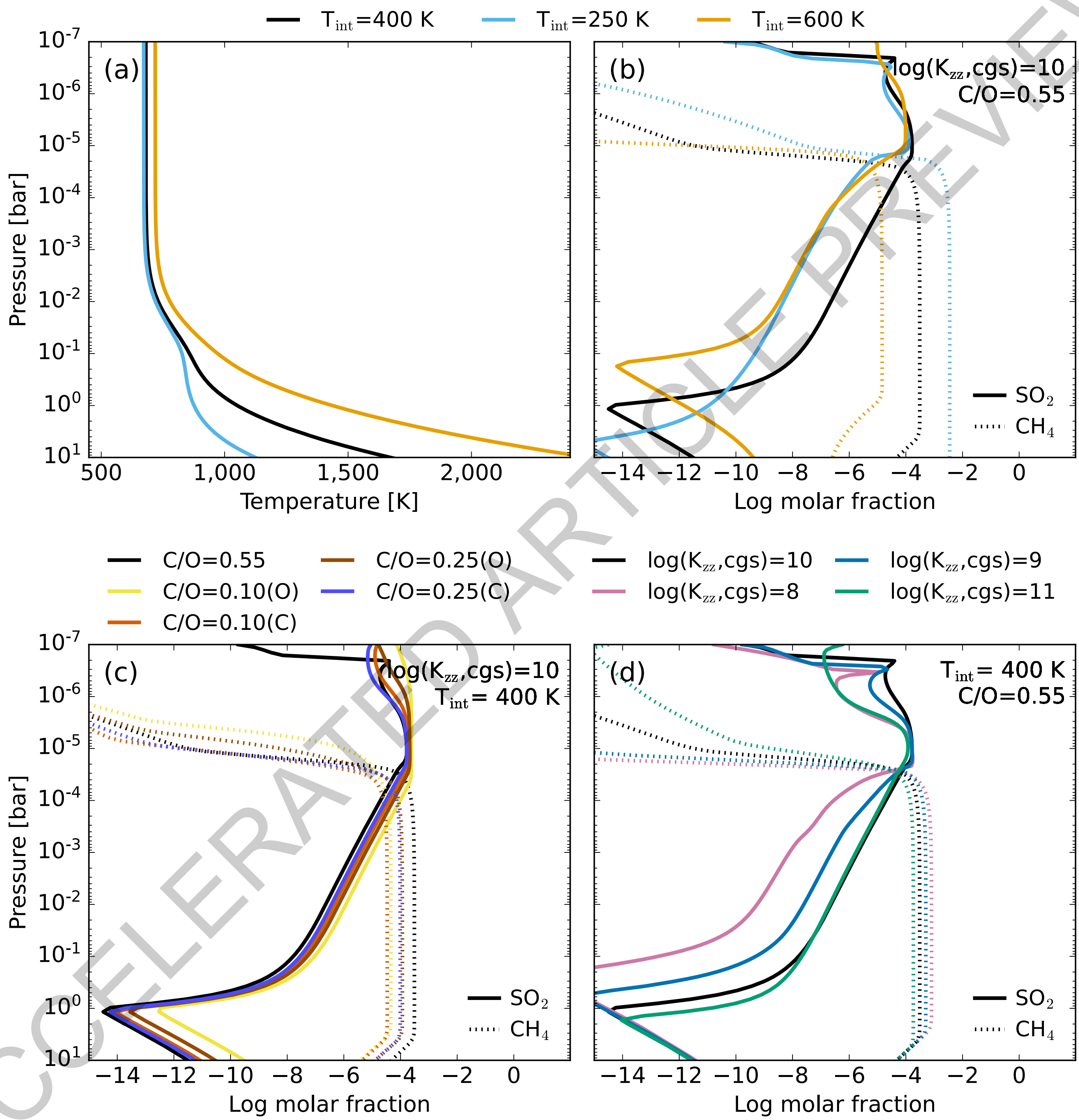

Extended Data Fig. 3

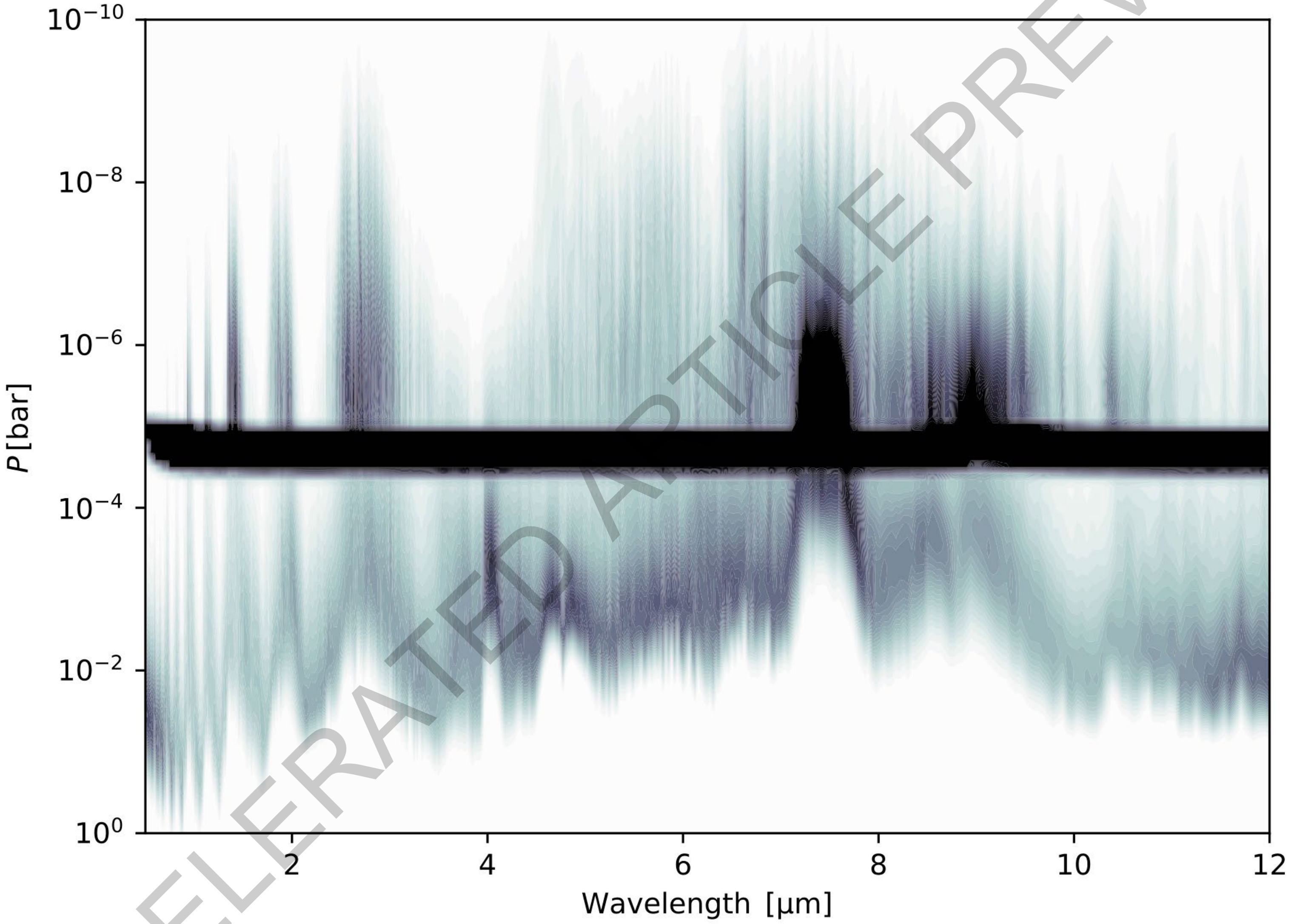

Extended Data Fig. 4

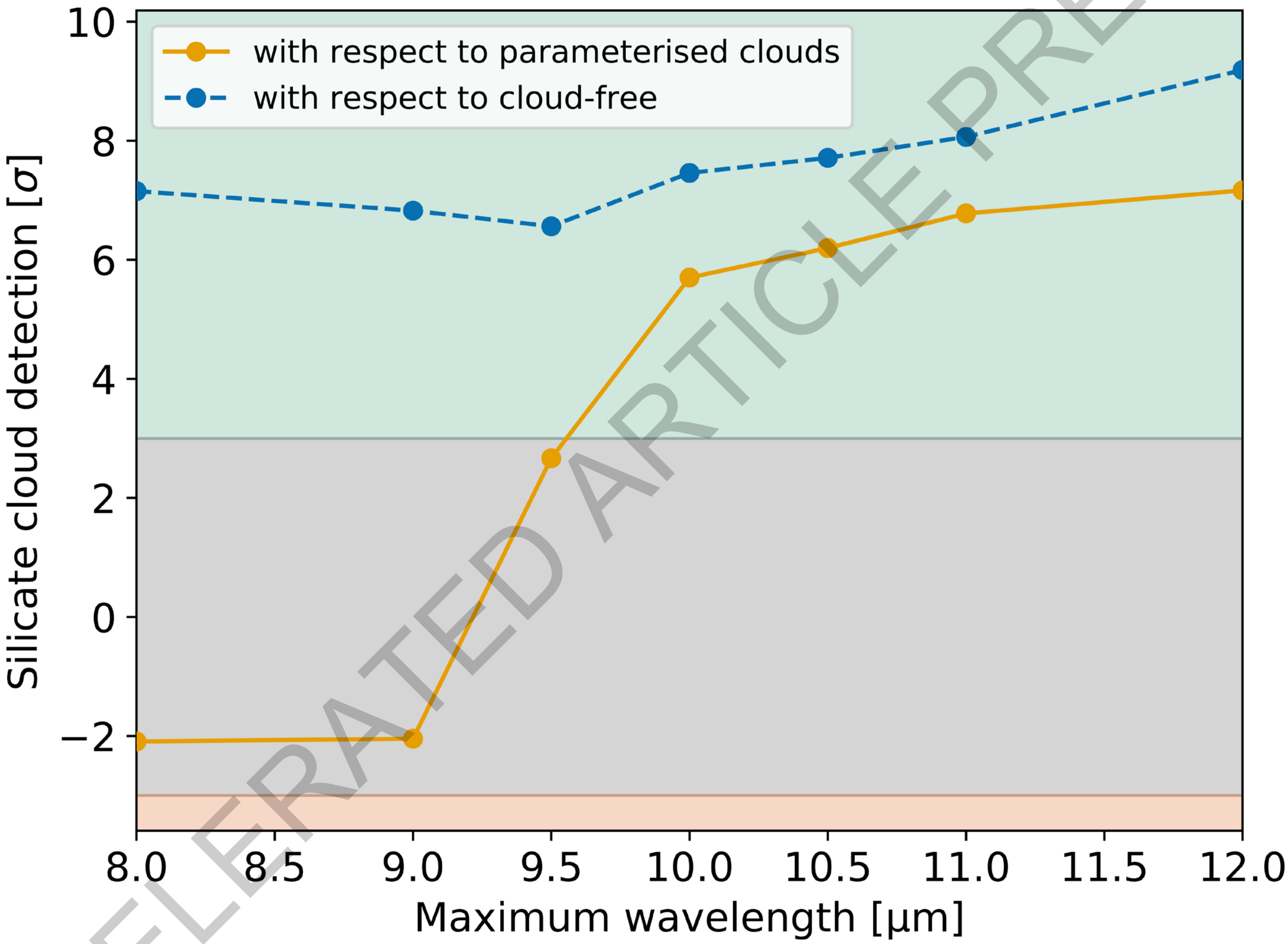

Extended Data Fig. 5

λ	Transit depth			λ	Transit depth		
	Eureka!	CASCADe	TEATRO		Eureka!	CASCADe	TEATRO
(μm)	(ppm)	(ppm)	(ppm)	(μm)	(ppm)	(ppm)	(ppm)
4.61	20,126 ± 80	20,305 ± 69	20,257 ± 73	8.37	20,813 ± 100	20,701 ± 87	20,811 ± 93
4.76	20,464 ± 60	20,233 ± 70	20,331 ± 52	8.52	20,745 ± 106	20,925 ± 99	20,727 ± 98
4.91	20,075 ± 73	20,223 ± 63	20,245 ± 70	8.67	21,095 ± 112	20,800 ± 96	20,850 ± 99
5.06	20,245 ± 60	20,128 ± 64	20,139 ± 53	8.82	20,725 ± 108	20,818 ± 96	20,733 ± 95
5.21	20,178 ± 60	20,192 ± 64	20,077 ± 52	8.97	20,603 ± 118	20,620 ± 100	20,350 ± 112
5.36	20,396 ± 55	20,154 ± 63	20,306 ± 46	9.12	20,807 ± 118	20,750 ± 114	20,654 ± 107
5.51	20,272 ± 69	20,227 ± 70	20,206 ± 58	9.27	20,447 ± 125	20,724 ± 114	20,523 ± 114
5.67	20,274 ± 65	20,326 ± 72	20,292 ± 53	9.42	20,562 ± 132	20,590 ± 110	20,411 ± 122
5.82	20,530 ± 76	20,329 ± 67	20,396 ± 65	9.57	20,475 ± 137	20,775 ± 111	20,676 ± 127
5.97	20,234 ± 64	20,196 ± 66	20,186 ± 55	9.72	20,466 ± 127	20,725 ± 117	20,574 ± 122
6.12	20,243 ± 68	20,217 ± 72	20,258 ± 59	9.87	20,512 ± 149	20,537 ± 94	20,460 ± 141
6.27	20,240 ± 66	20,166 ± 64	20,118 ± 61	10.02	20,166 ± 148	20,190 ± 134	20,190 ± 139
6.42	20,733 ± 66	20,567 ± 78	20,544 ± 55	10.17	20,539 ± 174	20,535 ± 110	20,584 ± 154
6.57	21,045 ± 77	20,945 ± 73	21,006 ± 65	10.32	20,404 ± 186	20,384 ± 125	20,109 ± 165
6.72	20,799 ± 67	20,720 ± 74	20,853 ± 58	10.47	20,580 ± 192	20,789 ± 164	20,406 ± 189
6.87	20,301 ± 79	20,364 ± 74	20,351 ± 73	10.62	20,606 ± 213	20,792 ± 186	20,462 ± 219
7.02	20,555 ± 72	20,420 ± 47	20,475 ± 65	10.77	20,062 ± 208	20,558 ± 172	19,853 ± 226
7.17	21,076 ± 78	20,993 ± 73	21,044 ± 69	10.92	19,600 ± 266	20,133 ± 223	19,618 ± 282
7.32	21,128 ± 76	21,093 ± 77	20,985 ± 71	11.07	20,239 ± 262	19,923 ± 260	19,742 ± 294
7.47	21,486 ± 88	21,351 ± 79	21,390 ± 77	11.22	19,474 ± 278	19,909 ± 282	18,938 ± 316
7.62	21,257 ± 83	21,160 ± 83	21,117 ± 73	11.37	18,810 ± 295	19,496 ± 295	18,371 ± 339
7.77	20,797 ± 100	20,817 ± 86	20,880 ± 85	11.52	19,101 ± 328	19,057 ± 291	18,625 ± 378
7.92	20,782 ± 93	20,762 ± 87	20,697 ± 81	11.68	19,157 ± 363	19,464 ± 369	18,963 ± 404
8.07	20,554 ± 90	20,587 ± 101	20,524 ± 83	11.83	18,994 ± 397	19,522 ± 396	18,459 ± 457
8.22	20,617 ± 98	20,688 ± 82	20,601 ± 89		–	–	–

Extended Data Table 1